

# Finite-range pairing in nuclear density functional theory

Sudhanva Lalit ,<sup>1</sup> Paul-Gerhard Reinhard ,<sup>2</sup> Kyle Godbey ,<sup>1</sup> and Witold Nazarewicz ,<sup>1,3</sup>

<sup>1</sup>*Facility for Rare Isotope Beams, Michigan State University, East Lansing, MI 48824, USA*

<sup>2</sup>*Institut für Theoretische Physik II, Universität Erlangen-Nürnberg, 91058 Erlangen, Germany*

<sup>3</sup>*Department of Physics and Astronomy, Michigan State University, East Lansing, Michigan 48824, USA*

Pairing correlations are ubiquitous in low-energy states of atomic nuclei. To incorporate them within nuclear density functional theory, often used for global computations of nuclear properties, pairing functionals that generate nucleonic pair densities and pairing fields are introduced. Many pairing functionals currently used can be traced back to zero-range nucleon-nucleon interactions. Unfortunately, such functionals are plagued by deficiencies that become apparent in large model spaces that contain unbound single-particle (continuum) states. In particular, the underlying computational schemes diverge as the single-particle space increases, and the results depend on how marginally occupied states are incorporated. These problems become more pronounced for pairing functionals that contain gradient-density dependence, such as in the Fayans functional. To remedy this, finite-range pairing functionals are introduced. In this study, this is done by folding the pair density with Gaussians. We show that a folding radius of about 1 fm offers the best compromise between quality and stability, and substantially reduces the pathological behavior in different numerical applications.

## I. INTRODUCTION

Shortly after the development of the Bardeen–Cooper–Schrieffer (BCS) theory of electronic superconductivity [1], nucleonic pairing was introduced [2–5]. Early pairing models employed a very simple ansatz for the pairing functional, such as the constant-gap or the constant-force monopole pairing model. With the advent of nuclear density functional theory (DFT) [6, 7], local density-dependent pairing functionals were proposed based on a zero-range pairing interaction [8–16]. In the following, we shall refer to such pairing functionals as “zero-range pairing functionals.”

While zero-range pairing functionals offer significant computational advantages, they give rise to ultraviolet divergences [17, 18]. Thus, zero-range pairing functionals come with a recipe for a high-momentum pairing cutoff, resulting in an effective pairing renormalization [19, 20]. An alternative to cope with the divergence is the pairing regularization developed in analogy to well-established regularization schemes in field theory [18, 21–25]. Although formally appealing, pairing regularization is plagued by problems similar to standard pairing cutoff schemes. Even worse, pairing functionals with gradient terms, as in the Fayans functionals [13, 14, 26], exhibit higher-order divergences which would require higher-order regularization. Particular problems arise as soon as high-energy continuum states are present in the Hartree-Fock-Bogoliubov (HFB) scheme.

Most HFB solvers rely on a finite basis representation, thus delivering a discretized approximation to the continuum. The structure of such a pseudo-continuum depends on the actual numerical representation (harmonic oscillator basis or coordinate-space grid, symmetry restrictions), numerical parameters [22, 23, 27, 28], and beyond mean-field corrections. As a consequence, pairing functionals are not fully portable between different HFB implementations. Particularly sensitive to various

approximations are the BCS calculations. The HFB pairing is a bit more robust because of the localization of canonical states [19]. This calls for pairing functionals that are intrinsically convergent. One possible solution is to replace zero-range functionals with finite-range ones. Finite-range pairing functionals have already been used in nuclear DFT calculations. A commonly used D1S Gogny functional [29–31] is a good example. A simplification of the Gogny pairing functional, which is particularly useful for numerical applications, is the separable pairing functional [32–37] which also involves a finite-range pairing. The present work continues along these lines.

This study explores separable pairing functionals in connection with non-relativistic nuclear DFT models, the widely used Skyrme functional, and, more importantly, the Fayans functional. The paper is structured as follows. In Sec. II, we briefly review the limitations of the zero-range pairing functionals. Section III introduces the finite-range pairing functional in the form used here. Results are presented in Sec. IV, which illustrates the performance of the new functional and presents the results of large-scale calibration to nuclear ground-state data. Finally, Sec. V contains the conclusions of this work.

## II. ZERO-RANGE PAIRING AND CONTINUUM EFFECTS

In this section, we discuss the effects of the continuum space in the standard BCS and HFB treatment of pairing with zero-range functionals. To limit the space of single-particle (s.p.) states used in the pairing equations, we employ here and throughout this paper a soft cutoff regulated by the s.p. energies, see Appendix A 2 for details.

### A. Box size dependence

The BCS approximation becomes sensitive to the size of the numerical expansion basis when many continuum states come into play [38]. This manifests in coordinate-space calculations primarily as a dependence on the numerical box size and grid spacing. Since the continuum is artificially discretized due to a finite box size, the density of the discretized states increases with increasing box size and effectively enhances the pairing strength logarithmically [19, 39]. The effect is marginal in calculations that use a small pairing cutoff with well-bound nuclei, as the continuum states contribute little in that case. For larger pairing cutoffs and/or weakly bound nuclei, this effect grows and introduces a considerable numerical uncertainty. In HFB calculations, however, the continuum states are localized, resulting in a weaker dependence on the size of the box.

### B. Localization of HFB canonical states

The set of canonical single-particle (s.p.) wave functions  $\varphi_\alpha$  is determined in the canonical representation by solving a system of coupled mean-field equations and taking the orthonormality of canonical states into account. The constrained variation of the total energy with respect to  $\varphi_\alpha^\dagger$  results in the HFB mean-field Hamiltonian [19, 28, 40, 41]

$$\hat{h}_{\text{HFB},\alpha} = \hat{h}_{\text{mf}} + \frac{u_\alpha}{v_\alpha} \hat{h}(\mathbf{r}), \quad (1a)$$

where  $\hat{h}_{\text{mf}}$  is the standard mean-field Hamiltonian,  $\hat{h}(\mathbf{r})$  is the pairing potential, and  $u_\alpha$ ,  $v_\alpha$  are the canonical occupation amplitudes. Note that, similar to Ref. [28], the pairing-rearrangement term is treated as part of the mean-field Hamiltonian. The canonical s.p. energy and the canonical s.p. pairing gap are:

$$\varepsilon_\alpha = \langle \varphi_\alpha | \hat{h}_{\text{mf}} | \varphi_\alpha \rangle \quad \text{and} \quad \Delta_{\alpha\alpha} = \left| \langle \varphi_\alpha | \hat{h}(\mathbf{r}) | \varphi_\alpha \rangle \right|, \quad (1b)$$

respectively. The gap equation

$$0 = 4v_\alpha(\varepsilon_\alpha - \varepsilon_F) + 2 \left( \frac{v_\alpha^2}{u_\alpha} - u_\alpha \right) \Delta_{\alpha\alpha}, \quad (1c)$$

where  $\varepsilon_F$  is the Lagrange multiplier for the particle number constraint (Fermi energy), is solved to get

$$\begin{Bmatrix} v_\alpha \\ u_\alpha \end{Bmatrix} = \sqrt{\frac{1}{2} \left( 1 \mp \frac{\varepsilon_\alpha - \varepsilon_F}{\sqrt{(\varepsilon_\alpha - \varepsilon_F)^2 + \Delta_{\alpha\alpha}^2}} \right)}. \quad (1d)$$

As the canonical continuum states are weakly occupied, i.e.,  $u_\alpha/v_\alpha \gg 1$ , the pairing potential in Eq. (1a) dominates, leading to localization given that  $\hat{h}(\mathbf{r}) \propto \check{\rho}(\mathbf{r})$

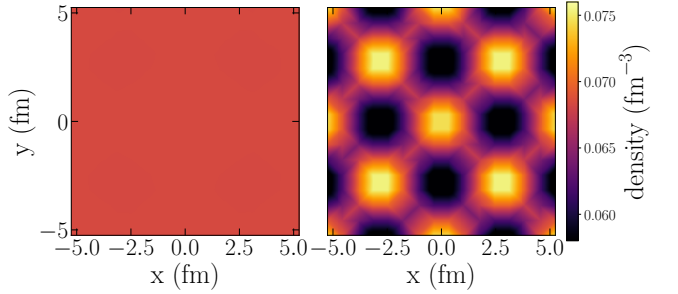


FIG. 1. Cut of the density distributions along  $x$ - and  $y$ -plane of a Fermi gas with density-dependent zero-range pairing simulated in a numerical box in three dimensions with box length 11.2 fm and with average density  $0.07/\text{fm}^3$ . The pairing parameters were taken from typical nuclear functionals and are  $V_{\text{prot}} = 601 \text{ MeV}/\text{fm}^3$ ,  $V_{\text{neut}} = 567 \text{ MeV}/\text{fm}^3$ , and switching density  $\rho_{0,\text{pair}} = 0.212/\text{fm}^3$ . The left panel shows the BCS result and the right panel the HFB result.

and the pairing density  $\check{\rho}$  is confined to the nucleus, mostly at the nuclear surface. This means that the pairing correlations are similarly confined. Far from the nucleus, pairing density vanishes, and continuum quasiparticles behave as free particles. Consequently, HFB calculations are less sensitive to the chosen box size [19, 23, 30, 31, 42].

This fact renders results practically independent of the size of the box, but creates a new problem: the pairing localization changes with the dimensionality and geometry of the implementation. In a 1D representation, the pairing potential is spherical and can localize only in the radial direction, thus representing a potential well on the surface of a sphere. In a 2D representation, the imposed axial symmetry causes the pairing potential to localize along the symmetry axis, which results in less spatial averaging and a deeper pairing potential well. In a Cartesian 3D code, even stronger localization is possible [28] given the unrestricted spatial symmetry.

A particular example of HFB localization can be seen for the case of infinite matter. To demonstrate this, we have simulated a Fermi gas with a density-dependent zero-range pairing functional

$$E_{\text{pair}} = \sum_{\text{nucl} \in \{\text{p}, \text{n}\}} \frac{V_{\text{nucl}}}{2} \int d^3r \left( 1 - \frac{\rho(\mathbf{r})}{\rho_{0,\text{pair}}} \right) \check{\rho}^*(\mathbf{r}) \check{\rho}(\mathbf{r}).$$

The resulting density distributions for BCS and HFB are shown in Fig. 1. BCS produces a perfectly homogeneous density distribution while HFB leads to a strong inhomogeneity. It shows up as a cubic lattice due to the cube-box boundary conditions. In infinite matter we expect that HFB will also break translational symmetry resulting in some crystalline structure. Experience from plasma physics suggests that the actual crystal symmetry depends on the density [43, 44].

The impact of dimensionality can be illustrated on the

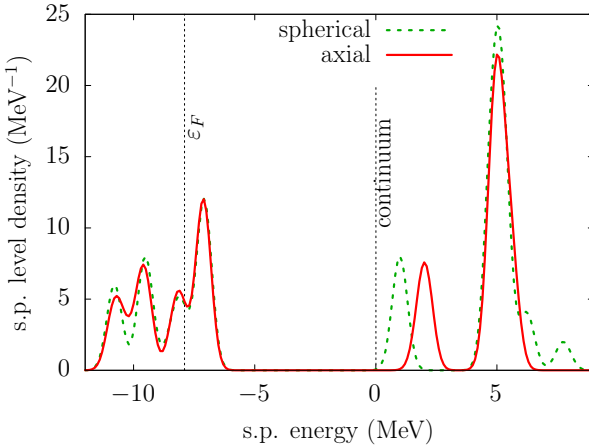


FIG. 2. Density of neutron s.p. states in  $^{120}\text{Sn}$  computed with HFB in spherical (dashed line) and axial (solid line) geometry using the functional Fy(IPV). The green dashed line shows the 1D spherical result and the red line the 2D axial result. The density of neutron s.p. states has been smoothed by a Gaussian of 0.5 MeV width to render the graphical representation better visible.

density of continuum canonical states, defined as

$$g(\varepsilon) = \sum_k \delta(\varepsilon - \varepsilon_k), \quad (2)$$

where  $\varepsilon_k$  is the energy of the  $k^{\text{th}}$  s.p. state. In practice, this is smoothed by a Gaussian to produce a continuous level-density function

$$\tilde{g}(\varepsilon) \approx \sum_k \frac{1}{\sqrt{\pi}\gamma} \exp\left(-\frac{(\varepsilon - \varepsilon_k)^2}{\gamma^2}\right), \quad (3)$$

where  $\gamma$  is the smoothing width parameter. Figure 2 shows the density of neutron s.p. states in  $^{120}\text{Sn}$  with respect to the s.p. energy using the 1D and 2D calculations. While the densities of bound states are similar, they show significant differences in the continuum region.

A strong HFB localization creates another problem: pairing isomerism from the state-wise pairing breakdown. This mechanism can be seen from the HFB Hamiltonian (1a). Small  $v_\alpha$  localizes the corresponding state, which, in turn, pushes the kinetic energy up and with it the s.p. energy (1b). A s.p. state may end up in a local energy minimum with  $v_\alpha = 0$ , leading to a pairing breakdown.

To illustrate this, we perform an HFB calculation with one chosen continuum state constrained to a given occupation  $v_\alpha^2$  and vary the constrained occupation systematically. The resulting energy curve is shown in Fig. 3. It has two minima: the ground state with finite  $v_\alpha$  and the excited minimum with vanishing occupation in the neutron  $2p_{1/2}$  state. This is only one of the many conceivable isomers in the continuum. This makes large-scale canonical-HFB calculations cumbersome because one has to check solutions for possible isomerism. The expectation is that a softer localization, with localized s.p. wave

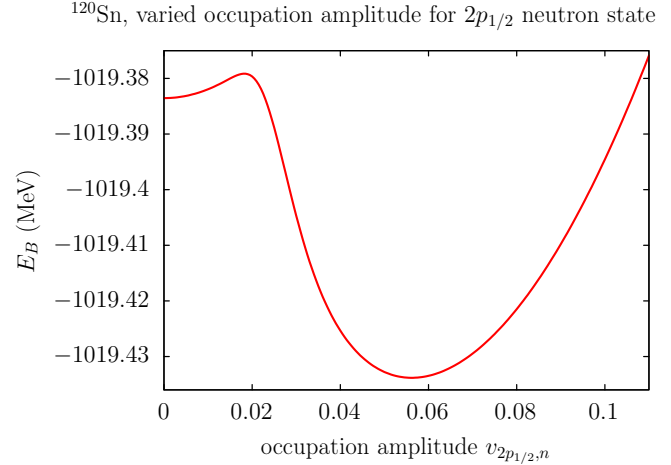


FIG. 3. Total energy of  $^{120}\text{Sn}$  computed with the functional SV-bas and HFB pairing as a function of constrained occupation amplitude  $v_\alpha$  for the neutron  $2p_{1/2}$  state which lies in the continuum.

functions that decay more slowly and have longer tails, keeps the kinetic energy lower and helps avoid the state-wise pairing breakdown.

### III. PAIRING FUNCTIONAL WITH FINITE RANGE

#### A. Formalism

To achieve an efficient computational scheme, we propose a separable approach, formulated in terms of an energy density functional (here: for time-reversal symmetric systems) with the pairing functional:

$$E_{\text{pair}} = \frac{1}{2} \int d^3r V(\rho(\mathbf{r})) \check{\rho}_{\mathcal{F}}^*(\mathbf{r}) \check{\rho}_{\mathcal{F}}(\mathbf{r}), \quad (4)$$

where the local pairing interaction  $V(\rho(\mathbf{r}))$  can be density-dependent, including gradient-density terms. The pairing density  $\check{\rho}_{\mathcal{F}}(\mathbf{r})$  in (4) is given by:

$$\check{\rho}_{\mathcal{F}}(\mathbf{r}) = \sum_{\alpha>0} u_\alpha v_\alpha \left( \hat{\mathcal{F}} \varphi_\alpha \right)^\dagger(\mathbf{r}) \left( \hat{\mathcal{F}} \varphi_\alpha \right)(\mathbf{r}), \quad (5)$$

where the folding Hermitian operator  $\hat{\mathcal{F}}$  can either be given in an integral form:

$$\left( \hat{\mathcal{F}} \varphi_\alpha \right)(\mathbf{r}) = \int d^3r' F(\mathbf{r} - \mathbf{r}') \varphi_\alpha(\mathbf{r}'), \quad (6)$$

where  $F$  is the folding function, or as a differential operator associated with the momentum operator  $\hat{\mathbf{p}}$ :

$$\left( \hat{\mathcal{F}} \varphi_\alpha \right)(\mathbf{r}) = \tilde{F}(\hat{\mathbf{p}}) \varphi_\alpha(\mathbf{r}) \quad (7)$$

with

$$\tilde{F}(\mathbf{p}) = \int d^3r e^{i\mathbf{p}\cdot\mathbf{r}} \mathcal{F}(\mathbf{r}). \quad (8)$$

Here and in the following, we adopt natural units with  $\hbar = 1$ .

The variation with respect to  $u_\alpha, v_\alpha$  together with the hermiticity of  $\hat{\mathcal{F}}$  yield the folded pairing potential:

$$\hat{h}_{\mathcal{F}}(\mathbf{r}) = \hat{\mathcal{F}}V(\mathbf{r})\check{\rho}_{\mathcal{F}}(\mathbf{r})\hat{\mathcal{F}} \quad (9)$$

and the state-dependent pairing gap

$$\Delta_\alpha = \int d^3r \varphi_\alpha^\dagger \hat{h}_{\mathcal{F}}(\mathbf{r}) \varphi_\alpha. \quad (10)$$

The state-dependent s.p. HFB Hamiltonian now becomes

$$\hat{h}_{\text{HFB},\alpha} = \hat{h}_{\text{mf}} + \frac{u_\alpha}{v_\alpha} \hat{h}_{\mathcal{F}}(\mathbf{r}), \quad (11)$$

where the pairing potential  $\hat{h}(\mathbf{r})$  in Eq. (1a) has been replaced by  $\hat{h}_{\mathcal{F}}(\mathbf{r})$ .

The pairing energy (4) employs the folded pairing density  $\check{\rho}_{\mathcal{F}}$  that contains two convoluted wave functions. This means that the present finite-range ansatz employs a fourfold separability. The advantage of this prescription is that it combines momentum conservation with the simple expression (4) for the pairing density functional. The twofold separable ansatz of Ref. [34] requires an additional  $\delta$ -function for momentum conservation, which, in turn, inhibits a simple reduction to an energy-density functional.

For the folding prescription, we adopt the Gaussian folding:

$$\mathcal{F}(\mathbf{r}) \propto \exp\left(-\frac{\mathbf{r}^2}{\tilde{R}_{\mathcal{F}}^2}\right) \quad \longleftrightarrow \quad \tilde{F} \propto \exp\left(-\frac{\tilde{R}_{\mathcal{F}}^2}{4}\hat{\mathbf{p}}^2\right). \quad (12)$$

Gaussian folding functions offer several advantages. In grid representations, they allow for an efficient implementation by factorizing the Gaussians in any orthogonal coordinate system. While not employed in the current work, the Gaussian form is also well suited to the oscillator basis representation, making it beneficial to many HFB production codes. However, it should be noted that Fourier transformations (backwards and forwards) can get expensive depending on grid size. For the implementation on a 1D spherical grid, we apply folding as a matrix operation (see Appendix C for details).

## B. Optimization of functionals

Using the prescription given in Sec. III A, we now attempt to quantify how the finite HFB folding radius affects the quality of a functional. To check this, we have

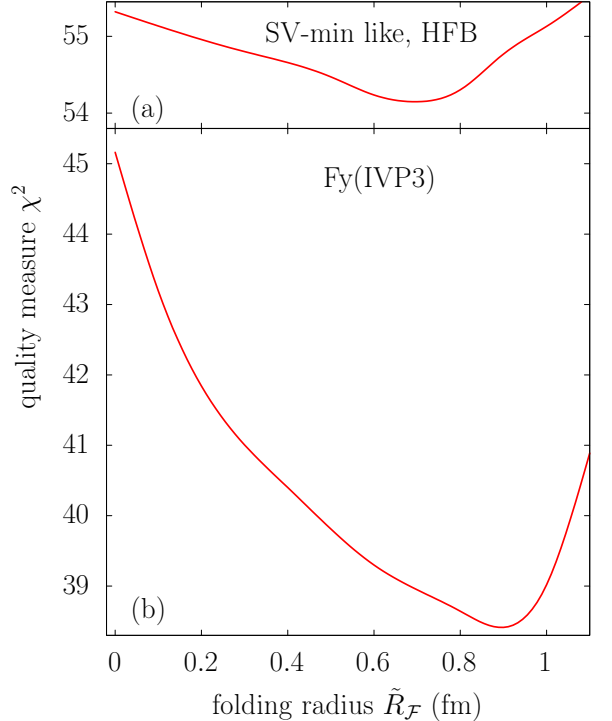


FIG. 4. The global quality measure  $\chi^2$  as a function of the folding radius for two functionals: (a) Skyrme EDF and (b) Fayans EDF Fy(IPV3). Both EDFs were optimized with a cutoff in pairing space of  $E_{\text{cut}} = 15$  MeV.

performed  $\chi^2$  fits with systematically varied folding radius. The calibration was done exactly in the same manner as for the corresponding zero-range functionals. For the Skyrme functional with finite-range pairing, we used the calibration dataset of SV-min, which consists of binding energies, r.m.s. charge radii, box-equivalent radii, and surface thicknesses for a selection of semi-magic nuclei from  $^{16}\text{O}$  up to  $^{218}\text{U}$  complemented by pairing gaps and spin-orbit splittings in doubly-magic nuclei. For more details, see Ref. [45]. For Fayans functionals, we used the same data set as Fy(IPV), which consists of the SV-min dataset with additional information on radius differences in Ca, Sn, and Pb isotopes[46–48]. For both functionals, the fits were done at the HFB level with a soft pairing cutoff of 15 MeV. The resulting quality measure  $\chi^2$  is shown in Fig. 4. The patterns are similar for both functionals: there is a preference for moderate folding radii between 0.7 and 0.9 fm. In Appendix B we provide the resulting functional parameters at the  $\chi^2$  minimum for both cases:  $\tilde{R}_{\mathcal{F}} = 0.7$  fm for the Skyrme functional and 0.9 fm for the Fayans functional. The variation is rather small for the Skyrme calibration (upper panel), but Fy(IPV3) benefits substantially from a finite folding radius.

## IV. RESULTS

For our tests, we choose  $^{120}\text{Sn}$ , which has a closed proton shell (thus no proton pairing) and an open neutron shell. We use the SV-bas mean-field parametrization [45] as a baseline for the EDF. In Appendix A we provide the details of the functionals used in this work. Note that the published neutron pairing strength applies only to a soft cutoff with the scheme as specified in Ref. [45]. In our case, the neutron pairing strength changes dramatically with pairing scheme, cutoff, and folding radius. Thus, we must adjust it to the given folding parameters and cutoff energies, as an isolated change in model parameters (here, the folding radius) can compromise the quality of the fit. For example, if the neutron pairing strength for folding radius  $\tilde{R}_F = 0$  is  $317 \text{ MeV fm}^2$ , it becomes  $4340 \text{ MeV fm}^2$  for  $\tilde{R}_F = 1.5 \text{ fm}$  and  $26700 \text{ MeV fm}^2$  for  $\tilde{R}_F = 3 \text{ fm}$ . Unless otherwise specified, the other parameters of the functional used in this section were kept at the values optimized at  $\tilde{R}_F = 0 \text{ fm}$ .

### A. Impact of folding range on observables

Figure 5 shows trends of observables for four different cases: BCS at  $\tilde{R}_F = 0$ , and HFB at  $\tilde{R}_F = 0, 1$ , and  $2 \text{ fm}$ . The left panels show the distribution of s.p. radii as a function of the s.p. energy. The colors of the points indicate the orbital angular momentum  $\ell$  of a state. For the BCS case with the zero folding radius, the s.p. radii show a marked change at the continuum threshold. Below, they grow steadily with increasing s.p. energy, while at the threshold, they jump to large values. The continuum states with radii around  $15 \text{ fm}$  extend over the numerical box, while a few states have smaller radii. These are weakly localized continuum resonances.

The HFB calculations produce a different trend. At zero folding, all s.p. radii are below  $6 \text{ fm}$ . This is due to strong localization produced by the  $u/v$  contribution in the HFB Hamiltonian (Eq. 1a) [19, 46, 49]. Increasing folding radius, weakens the localization until it is practically lost for  $\tilde{R}_F = 2 \text{ fm}$ . With few exceptions, the s.p. radii of the unbound states increase with  $\ell$ , which is an effect of the centrifugal term. It is interesting to note that HFB localization, which is strong for  $\tilde{R}_F = 0$  and still appreciable for  $\tilde{R}_F = 1 \text{ fm}$ , pushes the high- $\ell$  states to higher energies beyond those shown.

The right panels of Fig. 5 show the distribution of s.p. neutron pairing gaps  $\Delta_\alpha$ . The pairing gaps generally increase up to the zero-energy continuum threshold. Above the threshold, most of the BCS gaps drop quickly down to very small values, with a few remaining at moderate values for the localized continuum resonances. The trends in gaps also show a marked change with the folding radius in relation to the changes in radii. In the HFB variant at  $\tilde{R}_F = 0$ , the continuum states have large gaps because all these states are well localized and the interaction is independent of s.p. energy. A nonzero finite

folding radius leads to a decrease in the interaction with increasing kinetic energy. This is seen for the two cases with non-zero folding radii. For  $\tilde{R}_F = 1 \text{ fm}$ , pairing gaps vary smoothly across the threshold, while for  $\tilde{R}_F = 2 \text{ fm}$ , there appears a sharp threshold peak.

The results shown in Fig. 5 suggest that large folding radii are disadvantageous. On the other hand, folding radii around  $\tilde{R}_F = 1 \text{ fm}$  promise a fair compromise between convergence, soft localization, and smooth trends in physical properties.

A word is in order about the HFB isomers discussed around Fig. 3 and often seen in connection with zero-range pairing. The BCS calculations are free of that problem. However, in HFB calculations with zero folding radius, pairing isomers are likely to develop (see Fig. 3). This is not the case for larger folding radii: in our calculations, we did not find HFB isomers for  $\tilde{R}_F \geq 0.5 \text{ fm}$ .

The cutoff energy  $\epsilon_{\text{cut}}$  in pairing space controls the number of active s.p. states  $N_{\text{st}}$  to be included in the calculation [50]. In this section, we check the convergence of the results with increasing pairing space. We expect that a combination of the cutoff energy with a finite folding radius would improve the convergence.

### B. Dependence on the size of pairing space

Even though finite-range pairing renders the summations over s.p. states convergent, they still may converge slowly, thus requiring very many s.p. states. Practical considerations often suggest to limit their number. The first measure is technical; one limits the number of s.p. states in the calculations, either by number or by maximum s.p. energy. However, this hard cutoff can lead to fluctuations in the results when changing the numerical representation, the nucleus, or its deformation. To avoid this, a soft cutoff is used in a second step, as described in Sec. A 2. Here, we investigate the impact of the number of active states on the results.

Figure 6 shows the dependence of the charge radius and pairing energy in the spherical  $^{120}\text{Sn}$  on the cube root of the number of states  $N_{\text{st}}$  for  $\epsilon_{\text{cut}} = 45 \text{ MeV}$ . The deviations are significant at the smallest pairing spaces. The worst case is that of BCS at zero folding radius. At  $\tilde{R}_F = 1 \text{ fm}$ , the fluctuations are reduced by an order of magnitude.

In addition, we have also investigated a case of deformed  $^{170}\text{Yb}$  using the SkyAx code [50], which employs a cylindrical coordinate-space grid. While the convergence of results in this case is slower, we find in all respects the same behavior as for spherical nuclei. The dependence of total binding energy and charge radius on the size of pairing space in terms of  $N_{\text{st}}$  is demonstrated in Fig. 7. In these calculations, the folding radius was set to  $\tilde{R}_F = 1 \text{ fm}$ . The convergence is fast for cutoff energies up to  $40 \text{ MeV}$ . The largest cutoff of  $60 \text{ MeV}$  shows more  $N_{\text{st}}$ -dependence. However, one should keep in mind the scale: in the space above  $N_{\text{st}}^{1/3} = 9$ , the resulting error on the

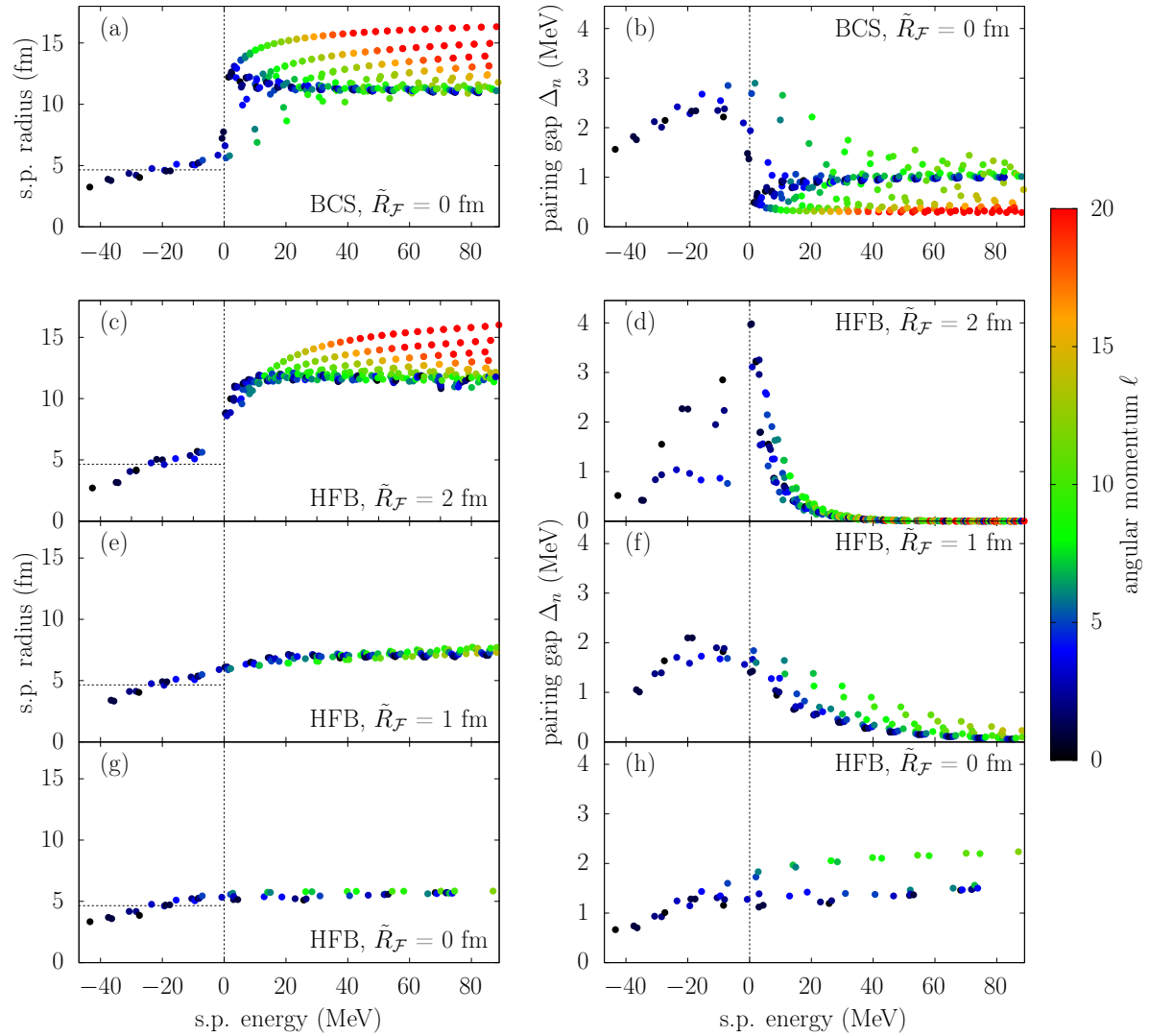


FIG. 5. Trends of key observables for BCS with  $\tilde{R}_F = 0$  (panels (a) and (b)) and HFB (panels (c)-(h)) for three different folding radii,  $\tilde{R}_F = 0, 1$ , and  $2$  fm as functions of s.p. energy. Test case is  $^{120}\text{Sn}$  computed with SV-bas and cutoff energy  $\varepsilon_{\text{cut}} = 100$  MeV. The orbital angular momentum  $\ell$  of the s.p. states is indicated by color code. Left panels: s.p. r.m.s. radii are plotted as a function of s.p. energy. The radius scale extends up to 18 fm, corresponding to the radius of the numerical box. Right panels: neutron s.p. pairing gaps  $\Delta_\alpha$  plotted as a function of s.p. energy. The faint vertical lines indicate the continuum threshold. The horizontal dotted line indicates the total charge r.m.s. radius of  $^{120}\text{Sn}$ .

radius remains below 0.0005 fm and it is below 0.1 MeV for the total energy; both are acceptable uncertainties for most practical applications.

### C. Cutoff dependence

Having answered the question of the number of states in the s.p. basis, we now discuss the impact of the cutoff energy. In all cases, we ensure that the number of states is always large enough to cover the given cutoff energy.

To illustrate the effect of the varying cutoff energy, Fig. 8 shows the charge radius and total HFB energy at

different folding radii as a function of  $\varepsilon_{\text{cut}}$ . To better illustrate the variation with cutoff, all observables are plotted relative to their value at  $\varepsilon_{\text{cut}} = 100$  MeV. The pairing strength has been calibrated for each folding radius to deliver the same pairing gap at  $\varepsilon_{\text{cut}} = 100$  MeV. The observables converge nicely with the increasing cutoff for the nonzero folding radii. An increase in the folding radius results in a faster convergence. No convergence is seen for  $\tilde{R}_F = 0$ , since pairing properties are known to diverge for zero-range pairing interactions [18, 51].

Although finite-range pairing creates an ultimately converging pairing scheme, the actual rate of convergence is moderate. It is only at large folding radii that one can

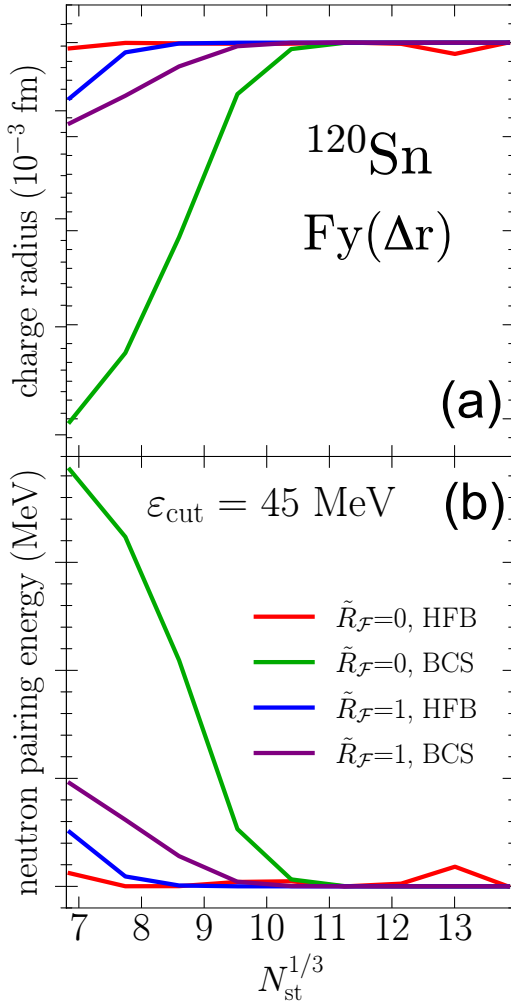


FIG. 6. (a) Charge radius and (b) neutron pairing energy in  $^{120}\text{Sn}$  versus size of pairing space  $N_{\text{st}}^{1/3}$  computed with  $\text{Fy}(\Delta r)$  EDF [26] with  $\varepsilon_{\text{cut}} = 45$  MeV. To visualize the variation, results are shown relative to the values obtained at the largest pairing space.

achieve near full convergence at cutoff energies of about 30 MeV. However, such large folding radii are excluded in calculations due to quality considerations (see Sec. III B).

#### D. Box-size dependence

In Sec. II A, we discussed the dependence of box size for BCS and HFB calculations with zero-range pairing. Here, we examine the changes associated with finite-range pairing. We concentrate on HFB and use a somewhat larger cutoff energy ( $\varepsilon_{\text{cut}} = 25$  MeV) to enhance the impact of continuum states. Figure 9 shows trends of two key observables, namely, the total binding energy, and the charge radius as a function of box size for various folding radii as indicated, using the SV-bas functional. All HFB results show occasional cusps. This indicates

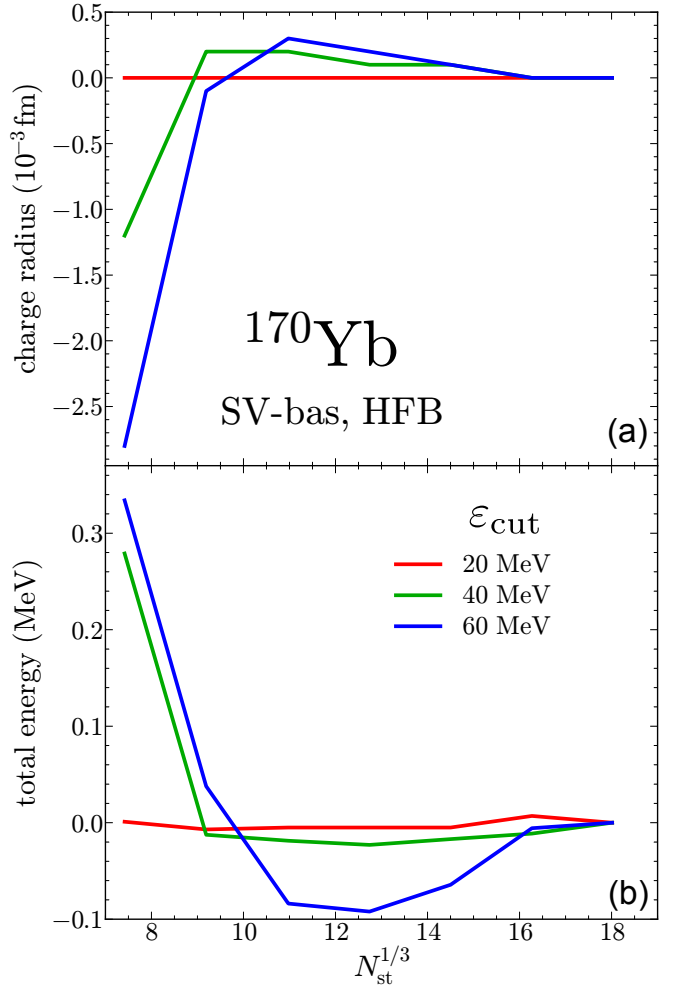


FIG. 7. (a) Charge radius and (b) total energy versus size of pairing space  $N_{\text{st}}^{1/3}$  of the deformed nucleus  $^{170}\text{Yb}$  for different cutoff energies computed with SV-bas and HFB. The folding radius is  $\tilde{R}_{\mathcal{F}} = 1$  fm.

that there is still a problem with HFB iterations being caught in a state-wise pairing isomerism. But the cusps are so small that the effects on the observables are insignificant. The case of  $\tilde{R}_{\mathcal{F}} = 1.0$  fm is as robust as the zero folding radius, though the situation worsens for larger radii. For a folding radius of 3 fm, we see a large box dependence in HFB for box radius  $\lesssim 33$  fm. This variation happens since the folding radius being too large reduces contribution from the continuum states, resulting in a numerical instability, similar to the BCS case. A large box size  $\gtrsim 33$  fm accounts for the continuum states resulting in converged solutions.

#### E. Portability

Another argument for introducing a finite folding radius in the pairing functional is that it helps to improve the portability between different numerical representa-

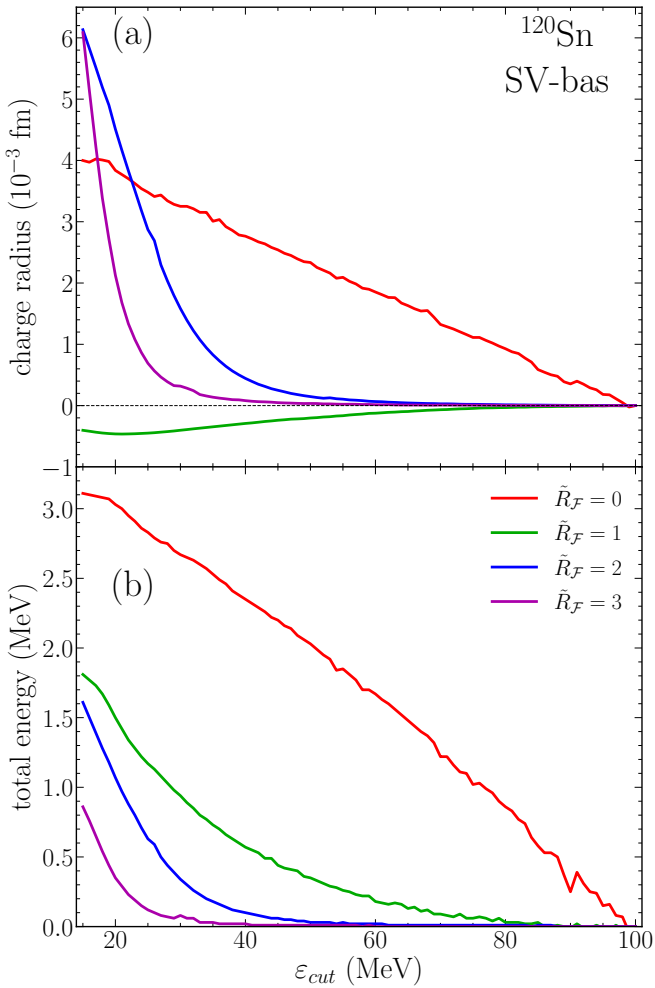


FIG. 8. (a) Charge radius and (b) total energy as a function of the cutoff energy  $\varepsilon_{\text{cut}}$  for  $^{120}\text{Sn}$  computed with SV-bas and HFB pairing for four different folding radii  $\tilde{R}_{\mathcal{F}}$  as indicated (in units of fm). The neutron pairing strength has been calibrated for each folding radius such that the pairing gap is the same at  $\varepsilon_{\text{cut}} = 100$  MeV. To emphasize the relative changes, all observables are scaled to zero at  $\varepsilon_{\text{cut}} = 100$  MeV.

tions. In Fig. 2, we demonstrated that a zero-range pairing functional can lead to different spectral distributions near continuum threshold. Fig. 10 applies the same analysis to a pairing functional with finite folding radius  $\tilde{R}_{\mathcal{F}} = 1.5$  fm. We see now a near-perfect agreement in the continuum region. The axial peak heights are slightly lower and their widths slightly broader because the strictly degenerated s.p. levels in the spherically symmetric grid are spread in an axial representation due to symmetry breaking. For the same reason, around -10 MeV, another broadening and slight shift is seen.

## V. CONCLUSIONS

In this work, we studied a finite range pairing functional based on the Gaussian folding of the canonical

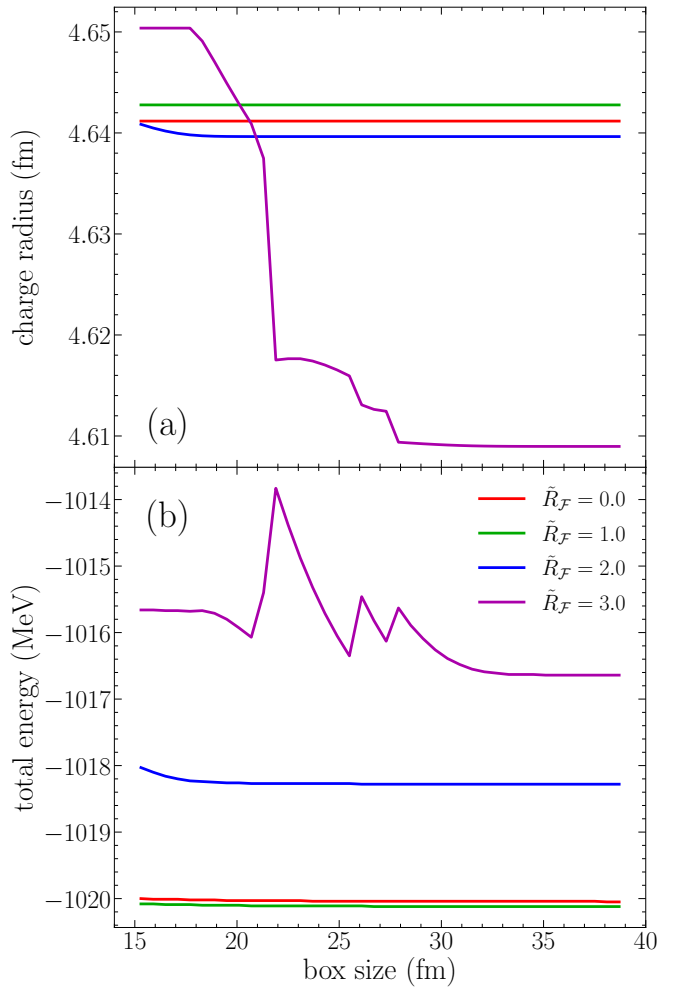


FIG. 9. (a) Charge radius and (b) total HFB energy versus box size computed at  $\varepsilon_{\text{cut}} = 25$  MeV with  $\tilde{R}_{\mathcal{F}} = 0, 1, 2$ , and 3 fm for the case of  $^{120}\text{Sn}$  using the SV-bas functional. The kinks for  $R_{\mathcal{F}} = 3$  are caused by unlocalized continuum states.

HFB wave functions entering the pairing density. The proposed formalism has been applied to two DFT models based on Skyrme and Fayans energy density functionals. When compared to BCS or HFB calculations with zero-range pairing, our finite-range pairing prescription allows one to choose lower cutoffs and thus smaller model spaces. The approach also helps avoid pairing isomer solutions associated with vanishing pairing, resulting in better convergence of HFB iterations. The finite-size pairing also improves the portability of the implementation between different spatial geometries.

We explored the effects of the size of the pairing space on the convergence of BCS and HFB calculations. The HFB calculations with non-zero folding radii converge well with increasing pairing space for both spherical and deformed nuclei. A combination of smaller folding radii ( $\sim 1$  fm) and cutoff energies ( $\sim 15$  MeV) is sufficient for an accurate and stable calculation. For large folding radii, such as  $\tilde{R}_{\mathcal{F}} = 3$  fm, the calculations show a strong box

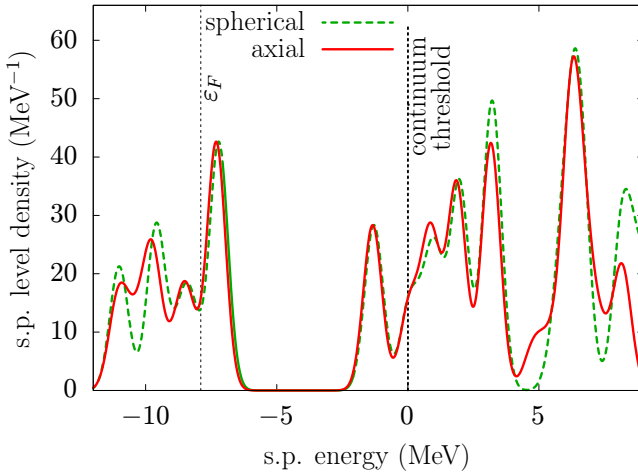


FIG. 10. Density of neutron s.p. states in  $^{120}\text{Sn}$  computed with HFB in spherical (dashed line) and axial (solid line) geometry using the functional SV-bas and a folding radius  $R_F = 1.5$  fm. The density of states has been smoothed by a Gaussian of 0.5 MeV width to render graphical representation better visible.

size dependence due to unlocalized s.p. states in continuum, similar to the benchmark BCS calculations.

Lastly, we have re-optimized the functionals with the finite folding radius and demonstrated a slightly enhanced calibration performance for both Skyrme and Fayans EDFs. The improved performance and stability of the new EDFs are promising for large-scale calculations of nuclear properties, and a systematic study exploring the performance on other observables is currently underway.

## ACKNOWLEDGEMENTS

Discussions with Ante Ravlić are gratefully appreciated. This material is based upon work supported by the U.S. Department of Energy under Award Numbers DE-SC0013365 and DE-SC0023688 (Office of Science, Office of Nuclear Physics), and DE-SC0023175 (Office of Science, NUCLEI SciDAC-5 collaboration). P.-G.R. acknowledges computing resources from the computing center of the University Erlangen/Nürnberg (RRZE).

## Appendix A: The functionals in detail

In this Appendix, we provide the details for the energy-density functionals used in this paper.

### 1. The local densities

Nuclear energy-density functionals are usually expressed in terms of a local densities and currents. As

we consider here only ground states of even-even nuclei, we can limit ourselves to the time-even densities: local density  $\rho$ , kinetic-energy density  $\tau$ , spin-orbit density  $\mathbf{J}$ , and pair density  $\check{\rho}$ . They read:

$$\rho_q(\mathbf{r}) = \sum_{\alpha \in q} f_{\alpha}^{(\text{cut})} v_{\alpha}^2 |\varphi_{\alpha}(\mathbf{r})|^2, \quad (\text{A1a})$$

$$\tau_q(\mathbf{r}) = \sum_{\alpha \in q} f_{\alpha}^{(\text{cut})} v_{\alpha}^2 |\nabla \varphi_{\alpha}(\mathbf{r})|^2, \quad (\text{A1b})$$

$$\mathbf{J}_q(\mathbf{r}) = -i \sum_{\alpha \in q} f_{\alpha}^{(\text{cut})} v_{\alpha}^2 \varphi_{\alpha}^+(\mathbf{r}) \nabla \times \hat{\sigma} \varphi_{\alpha}(\mathbf{r}), \quad (\text{A1c})$$

$$\check{\rho}_p(\mathbf{r}) = 2 \sum_{\alpha > 0, \alpha \in q} f_{\alpha}^{(\text{cut})} u_{\alpha} v_{\alpha} |\varphi_{\alpha}(\mathbf{r})|^2, \quad (\text{A1d})$$

where  $q = p$  or  $n$ . It is often useful to express densities in terms of isoscalar ( $T = 0$ ) and isovector ( $T = 1$ ) components. For instance:

$$\rho_{T=0} = \rho_p + \rho_n, \quad \rho_{T=1} = \rho_p - \rho_n. \quad (\text{A2})$$

### 2. Soft cutoff in s.p. space

The pairing occupation amplitude  $v_{\alpha}$  decreases slowly with s.p. energy  $\varepsilon_{\alpha}$ . Thus, the summations in (A1) do not converge if all s.p. states are considered. A possible way to remedy this problem is to apply a soft cutoff weight depending on s.p. energy  $\varepsilon_{\alpha}$  [12]:

$$f_{\alpha}^{(\text{cut})} = \frac{1}{1 + \exp [\varepsilon_{\alpha} - (\epsilon_F - \delta\epsilon)] / (\delta\epsilon/10)}, \quad (\text{A3})$$

where  $\delta\epsilon$  is the energy span of the pairing active zone above the Fermi surface.  $\delta\epsilon$  is a crucial cutoff parameter [50, 52]. Older calculations used 5 MeV, which embraces almost exclusively the bound states. The larger the cutoff, the more continuum states come into play.

### 3. The Skyrme energy functional

The Skyrme functional for time-even energy density can be written as [6]

$$E = \int d^3r \{ \mathcal{E}_{\text{kin}} + \mathcal{E}_{\text{Sk}} + \mathcal{E}_{\text{Sk,pair}} \} + E_{\text{Coul}} + E_{\text{cm}}, \quad (\text{A4})$$

where

$$\begin{aligned}
\mathcal{E}_{\text{kin}} &= \frac{\hbar^2}{2m} \tau, \\
\mathcal{E}_{\text{Sk},T} &= \sum_{T=0}^1 \left[ C_T^\rho \rho_T^2 + C_T^{\Delta\rho} \rho_T \Delta \rho_T \right. \\
&\quad \left. + C_T^\tau \rho_T \tau_T + C_T^J J_T^2 + C_T^{\nabla J} \rho_T \nabla \cdot \mathbf{J}_T \right], \\
\mathcal{E}_{\text{Sk,pair}} &= \frac{1}{4} \left[ 1 - \frac{\rho}{\rho_{\text{pair}}} \right] \sum_{q \in \{p,n\}} V_{0,q} \tilde{\rho}_q^2, \\
E_{\text{Coul}} &= e^2 \frac{1}{2} \iint d^3r d^3r' \frac{\rho_p(\mathbf{r}) \rho_p(\mathbf{r}')}{|\mathbf{r} - \mathbf{r}'|} \\
&\quad - \frac{3}{4} e^2 \left( \frac{3}{\pi} \right)^{1/3} \int d^3r \rho_p^{4/3}(\mathbf{r}), \\
E_{\text{cm}} &= -\frac{1}{2mA} \langle (\hat{P}_{\text{cm}})^2 \rangle, \quad \hat{P}_{\text{cm}} = \sum_i \hat{p}_i.
\end{aligned}$$

A density dependence in the Skyrme energy is included only in the volume term  $\propto \rho_T^2$ .

#### 4. The Fayans energy functional

Alternatively, we also discuss results obtained with the Fayans EDF [26]. The functional used in this work has a form where each of the three terms in the pairing functional is split into separate proton and neutron terms, each with its own strength coefficient. We abbreviate that as Fy(IPV3) to denote isospin variable pairing in all 3 terms. The functional reads:

$$\begin{aligned}
E &= \int d^3r \left\{ \mathcal{E}_{\text{kin}} + \mathcal{E}_{\text{Fy}}^v + \mathcal{E}_{\text{Fy}}^s + \mathcal{E}_{\text{Fy}}^{\text{ls}} + \mathcal{E}_{\text{Fy}}^{\text{pair}} \right\} \\
&\quad + E_{\text{Coul}} + E_{\text{cm}},
\end{aligned} \tag{A5}$$

where

$$\begin{aligned}
\mathcal{E}_{\text{Fy}}^v &= \frac{\varepsilon_F \rho_{\text{sat}}}{3} \left[ a_+^v \frac{1 - h_{1+}^v x_0^\sigma}{1 + h_{2+}^v x_0^\sigma} x_0^2 + a_-^v \frac{1 - h_{1-}^v x_0}{1 + h_{2-}^v x_0} x_1^2 \right], \\
\mathcal{E}_{\text{Fy}}^s &= \frac{\varepsilon_F \rho_{\text{sat}}}{3} \frac{a_+^s r_s^2 (\nabla x_0)^2}{1 + h_{\nabla}^s r_s^2 (\nabla x_0)^2}, \\
\mathcal{E}_{\text{Fy}}^{\text{ls}} &= \frac{4\varepsilon_F r_s^2}{3\rho_{\text{sat}}} (\kappa \rho_0 \nabla \cdot \mathbf{J}_0 + \kappa' \rho_1 \nabla \cdot \mathbf{J}_1), \\
\mathcal{E}_{\text{Fy}}^{\text{pair}} &= \frac{2\varepsilon_F}{3\rho_{\text{sat}}} \sum_{t=p,n} \tilde{\rho}_t^2 \left[ f_{\text{ex},t}^\xi + h_t^\xi x_{\text{pair}}^\gamma \right. \\
&\quad \left. + h_{\nabla,t}^\xi r_s^2 (\nabla x_{\text{pair}})^2 \right]
\end{aligned}$$

with  $x_T = \rho_T / \rho_{\text{sat}}$ . The Coulomb and c.m. terms are the same as in eq. (A4). Several model parameters are fixed a priori. These include the nucleon masses  $\hbar^2 / 2m_p = 20.749811 \text{ MeV fm}^2$ ,  $\hbar^2 / 2m_n = 20.721249 \text{ MeV fm}^2$ , the charge  $e^2 = 1.43996448 \text{ MeV fm}$ , the reference saturation density  $\rho_{\text{sat}} = 0.16 \text{ fm}^{-3}$ ,  $\rho_{\text{pair}} = \rho_{\text{sat}}$ ,  $\sigma = 1/3$ ,

and  $\gamma = 2/3$ . The saturation density  $\rho_{\text{sat}}$  also determines the auxiliary parameters, namely, the Wigner-Seitz radius  $r_s = (3/(4\pi\rho_{\text{sat}}))^{1/3} \text{ fm}$  and Fermi energy  $\varepsilon_F = (9\pi/8)^{2/3} \hbar^2 / 2mr_s^2 \text{ MeV}$ .

#### Appendix B: Calibrated EDF parameters

Table I shows the parameters for the Skyrme and the Fayans EDF with finite-range pairing at the minimum of the  $\chi^2$  curves in Fig. 4. The model parameters are complemented by the properties of symmetric nuclear matter at equilibrium (Table II). These help to characterize the basic physical properties of a functional.

	Skyrme	Fayans
$C_0^\rho$	-756.4018463	$a_+^v$ -9.608175465
$C_0^{\Delta\rho}$	430.0083542	$h_{1+}^v$ 0.6227052220
$D_0^\rho$	847.1928481	$h_{2+}^v$ 0.1726617465
$D_1^\rho$	-541.5625965	$a_-^v$ 2.2427483150*10 <sup>14</sup>
$C_0^{\Delta\rho}$	-53.13268906	$h_{1-}^v$ -2.316454053
$C_1^{\Delta\rho}$	-22.18923885	$h_{2-}^v$ 5.2906966945*10 <sup>14</sup>
$C_0^\tau$	6.218937572	$a_+^s$ 0.5483225953
$C_1^\tau$	3.648292998	$h_{\nabla}^s$ 0.3511339663
$C_0^{\nabla J}$	-77.76109200	$\kappa$ 0.1906406585
$C_1^{\nabla J}$	-18.57579450	$\kappa'$ -0.033380056233
$\alpha$	0.2745873647	$f_{\text{ex},p}^\xi$ -8.270525940
$V_{0,p}$	932.3973450	$h_p^\xi$ 7.304858433
$V_{0,n}$	899.6625795	$h_{\nabla,p}^\xi$ 5.666948816
$\rho_{\text{pair}}$	0.1987770272	$f_{\text{ex},n}^\xi$ -11.28934445
		$h_n^\xi$ 12.32075874
		$h_{\nabla,n}^\xi$ 8.428702197

TABLE I. Parameters of a Skyrme functional (left) and a Fayans functional (right) with finite-range pairing with  $\tilde{R}_{\mathcal{F}} = 0.7 \text{ fm}$  and  $\tilde{R}_{\mathcal{F}} = 0.9 \text{ fm}$  respectively, treated in HFB and pairing cutoff energy  $\varepsilon_{\text{cut}} = 15 \text{ MeV}$  at their minimum of the  $\chi^2$  curve in Fig. 4. All Skyrme parameters are given in units of MeV for energies and fm for lengths. The model parameters for the Fayans functional are dimensionless by construction.

Property	Skyrme	Fayans
$\rho_{\text{eq}} (\text{fm}^{-3})$	0.1603	0.1633
$E/A (\text{MeV})$	-15.903	-15.865
$K (\text{MeV})$	225.3	214.5
$m^*/m$	0.9541	1.000
$J (\text{MeV})$	30.35	29.97
$L (\text{MeV})$	38.74	61.83
$\kappa_{\text{TRK}}$	0.0206	0.0000

TABLE II. The nuclear matter properties of the parametrization, equilibrium density  $\rho_{\text{eq}}$ , binding energy per nucleon  $E/A$ , incompressibility  $K$ , isoscalar effective mass  $m^*/m$ , symmetry energy  $J$ , slope of symmetry energy  $L$ , and Thomas-Reiche-Kuhn sum rule enhancement  $\kappa_{\text{TRK}}$ .

### Appendix C: Construction of the folding matrix in a 1D spherical grid

The folding procedure for a 1D spherical representation involves the direct integration over the angles:

$$\begin{aligned}\mathcal{F}_l(r, r') &= \int d^2\Omega d^2\Omega' Y_{lm}^*(\Omega) \exp\left(-\frac{(\mathbf{r} - \mathbf{r}')^2}{\tilde{R}_{\mathcal{F}}^2}\right) Y_{lm}(\Omega') \\ &= 2\pi \int d\eta \exp\left(-\frac{r^2 + (r')^2 - 2rr'\eta}{\tilde{R}_{\mathcal{F}}^2}\right) P_l(\eta) \\ &= 2 \exp\left(-\frac{r^2 + (r')^2}{\tilde{R}_{\mathcal{F}}^2}\right) i_l\left(\frac{2rr'}{\tilde{R}_{\mathcal{F}}^2}\right)\end{aligned}$$

where  $\eta = \cos \vartheta$  and  $i_l$  is the modified Bessel function of the first kind.

Alternatively, one can carry out folding in the momentum representation by employing the Fourier-Bessel transformation:

$$\tilde{\mathcal{F}}(\mathbf{p}) \longrightarrow \tilde{\mathcal{F}}_{lm}(p) = \int dr r^2 d^2\Omega j_l(pr) Y_{lm}(\Omega) \mathcal{F}(\mathbf{r}). \quad (C1)$$

The  $p$  values are discretized to a set  $p_\nu^{(l)}$  on a finite  $l$ -dependent grid. The spatial folding can thus be represented as

$$\mathcal{F}_l(r, r') = \sum_\nu j_l(p_\nu r) \exp\left(-\frac{\tilde{R}_{\mathcal{F}}^2}{4} p_\nu^2\right) j_l(p_\nu r'). \quad (C2)$$

---

[1] J. Bardeen, L. N. Cooper, and J. R. Schrieffer, Microscopic theory of superconductivity, *Phys. Rev.* **106**, 162 (1957).

[2] A. Bohr, B. R. Mottelson, and D. Pines, Possible analogy between the excitation spectra of nuclei and those of the superconducting metallic state, *Phys. Rev.* **110**, 936 (1958).

[3] P. Ring and P. Schuck, *The Nuclear Many-Body Problem* (Springer-Verl., New York, Heidelberg, Berlin, 1980).

[4] D. J. Dean and M. Hjorth-Jensen, Pairing in nuclear systems: from neutron stars to finite nuclei, *Rev. Mod. Phys.* **75**, 607 (2003).

[5] R. A. Broglia and V. Zelevinsky, *Fifty Years of Nuclear BCS: Pairing in Finite Systems* (World Scientific, 2013).

[6] M. Bender, P.-H. Heenen, and P.-G. Reinhard, Self-consistent mean-field models for nuclear structure, *Rev. Mod. Phys.* **75**, 121 (2003).

[7] N. Schunck, ed., *Energy Density Functional Methods for Atomic Nuclei*, 2053-2563 (IOP Publishing, 2019).

[8] E. Sapershtein and M. Troitskiy, Sov. J. Nucl. Phys. **1**, 284 (1965).

[9] Z. Bochnacki, I. Holban, and I. Mikhailov, Residual interaction in nuclei, *Nucl. Phys. A* **97**, 33 (1967).

[10] R. R. Chasman, Density-dependent delta interactions and actinide pairing matrix elements, *Phys. Rev. C* **14**, 1935 (1976).

[11] S. G. Kadmenskiy, Y. L. Ratis, K. Rybak, and V. Furman, Choice of density-dependent effective interaction and  $\alpha$  decay of heavy spherical nuclei, Sov. J. Nucl. Phys. **27**, 481 (1978).

[12] S. J. Krieger, P. Bonche, H. Flocard, P. Quentin, and M. S. Weiss, An improved pairing interaction for mean-field calculations using Skyrme potentials, *Nucl. Phys. A* **517**, 275 (1990).

[13] S. Fayans, S. Tolokonnikov, E. Trykov, and D. Zawischa, Isotope shifts within the energy-density functional approach with density dependent pairing, *Phys. Lett. B* **338**, 1 (1994).

[14] S. Fayans and D. Zawischa, Towards a better parametrization of the nuclear pairing force: density dependence with gradient term, *Phys. Lett. B* **383**, 19 (1996).

[15] E. Garrido, P. Sarriuguren, E. Moya de Guerra, and P. Schuck, Effective density-dependent pairing forces in the  $T = 1$  and  $T = 0$  channels, *Phys. Rev. C* **60**, 064312 (1999).

[16] J. Dobaczewski, W. Nazarewicz, and P.-G. Reinhard, Pairing interaction and self-consistent densities in neutron-rich nuclei, *Nucl. Phys. A* **693**, 361 (2001).

[17] G. Bruun, Y. Castin, R. Dum, and K. Burnett, BCS theory for trapped ultracold fermions, *Eur. Phys. J. D* **7**, 433 (1999).

[18] A. Bulgac and Y. Yu, Renormalization of the Hartree-Fock-Bogoliubov equations in the case of a zero range pairing interaction, *Phys. Rev. Lett.* **88**, 042504 (2002).

[19] J. Dobaczewski, W. Nazarewicz, T. R. Werner, J. F. Berger, C. R. Chinn, and J. Dechargé, Mean-field description of ground-state properties of drip-line nuclei: Pairing and continuum effects, *Phys. Rev. C* **53**, 2809 (1996).

[20] T. Nikšić, P. Ring, and D. Vretenar, Renormalized relativistic Hartree-Bogoliubov equations with a zero-range pairing interaction, *Phys. Rev. C* **71**, 044320 (2005).

[21] Y. Yu and A. Bulgac, Energy density functional approach to superfluid nuclei, *Phys. Rev. Lett.* **90**, 222501 (2003).

[22] P. J. Borycki, J. Dobaczewski, W. Nazarewicz, and M. V. Stoitsov, Pairing renormalization and regularization within the local density approximation, *Phys. Rev. C* **73**, 044319 (2006).

[23] J. C. Pei, A. T. Kruppa, and W. Nazarewicz, Quasiparticle continuum and resonances in the hartree-fock-bogoliubov theory, *Phys. Rev. C* **84**, 024311 (2011).

[24] J. C. Pei, N. Fei, Y. N. Zhang, and P. Schuck, Generalized second-order Thomas-Fermi method for superfluid Fermi systems, *Phys. Rev. C* **92**, 064316 (2015).

[25] J. Dobaczewski and W. Nazarewicz, Hartree-Fock-Bogoliubov solution of the pairing Hamiltonian in finite nuclei, in *Fifty Years of Nuclear BCS*, edited by R. A. Broglia and V. Zelevinsky (World Scientific, 2013) p. 40.

[26] P.-G. Reinhard and W. Nazarewicz, Toward a global description of nuclear charge radii: Exploring the Fayans energy density functional, *Phys. Rev. C* **95**, 064328 (2017).

[27] J. C. Pei, M. V. Stoitsov, G. I. Fann, W. Nazarewicz,

N. Schunck, and F. R. Xu, Deformed coordinate-space hartree-fock-bogoliubov approach to weakly bound nuclei and large deformations, *Phys. Rev. C* **78**, 064306 (2008).

[28] M. Chen, T. Li, B. Schuetrumpf, P.-G. Reinhard, and W. Nazarewicz, Three-dimensional Skyrme Hartree-Fock-Bogoliubov solver in coordinate-space representation, *Comput. Phys. Commun.* **276**, 108344 (2022).

[29] J. Berger, M. Girod, and D. Gogny, Microscopic analysis of collective dynamics in low energy fission, *Nucl. Phys. A* **428**, 23 (1984).

[30] M. Grasso, N. Sandulescu, N. Van Giai, and R. J. Liotta, Pairing and continuum effects in nuclei close to the drip line, *Phys. Rev. C* **64**, 064321 (2001).

[31] M. Grasso, N. Van Giai, and N. Sandulescu, Continuum hfb calculations with finite range pairing interactions, *Phys. Lett. B* **535**, 103 (2002).

[32] T. Duguet, Bare vs effective pairing forces: A microscopic finite-range interaction for Hartree-Fock-Bogolyubov calculations in coordinate space, *Phys. Rev. C* **69**, 054317 (2004).

[33] Y. Tian, Z.-y. Ma, and P. Ring, Separable pairing force for relativistic quasiparticle random-phase approximation, *Phys. Rev. C* **79**, 064301 (2009).

[34] Y. Tian, Z.-y. Ma, and P. Ring, A finite range pairing force for density functional theory in superfluid nuclei, *Phys. Lett. B* **676**, 44–50 (2009).

[35] Z.-y. Ma, Y. Tian, and P. Ring, Density functional theory with a separable pairing force in finite nuclei, *Nucl. Phys. A* **834**, 50c (2010).

[36] P. Veselý, J. Dobaczewski, N. Michel, and J. Toivanen, Finite-range separable pairing interaction within the new N3LO DFT approach, *J. Phys.: Conf. Ser.* **267**, 012027 (2011).

[37] S. Teeti and A. V. Afanasjev, Global study of separable pairing interaction in covariant density functional theory, *Phys. Rev. C* **103**, 034310 (2021).

[38] A. Migdal, *Theory of Finite Fermi Systems and Applications to Atomic Nuclei*, Interscience monographs and texts in physics and astronomy (Interscience, New York, 1967).

[39] M. Brack, J. Damgaard, A. S. Jensen, H. C. Pauli, V. M. Strutinsky, and C. Y. Wong, Funny Hills: The shell-correction approach to nuclear shell effects and its applications to the fission process, *Rev. Mod. Phys.* **44**, 320 (1972).

[40] P. G. Reinhard, M. Bender, K. Rutz, and J. A. Maruhn, An HFB scheme in natural orbitals, *Z. Phys. A* **358**, 277 (1997).

[41] N. Tajima, Canonical-basis solution of the Hartree-Fock-Bogoliubov equation on a three-dimensional Cartesian mesh, *Phys. Rev. C* **69**, 034305 (2004).

[42] Y. N. Zhang, J. C. Pei, and F. R. Xu, Hartree-fock-bogoliubov descriptions of deformed weakly bound nuclei in large coordinate spaces, *Phys. Rev. C* **88**, 054305 (2013).

[43] T. Mitchell, J. Bollinger, X.-P. Huang, W. Itano, J. Tan, B. Jelenković, and D. Wineland, Crystalline order in strongly coupled ion plasmas, in *AIP Conf. Proc.*, Vol. 498 (1999) pp. 353–366.

[44] A. Piel, A. Homann, M. Klindworth, A. Melzer, C. Zafiu, V. Nosenko, and J. Goree, Waves and oscillations in plasma crystals, *J. Phys. B* **36**, 533 (2003).

[45] P. Klüpfel, P.-G. Reinhard, T. J. Bürvenich, and J. A. Maruhn, Variations on a theme by Skyrme: A systematic study of adjustments of model parameters, *Phys. Rev. C* **79**, 034310 (2009).

[46] A. J. Miller, K. Minamisono, A. Klose, D. Garand, C. Kujawa, J. D. Lantis, Y. Liu, B. Maaß, P. F. Mantica, W. Nazarewicz, W. Nörtershäuser, S. V. Pineda, P. G. Reinhard, D. M. Rossi, F. Sommer, C. Sumithrachchi, A. Teigelhöfer, and J. Watkins, Proton superfluidity and charge radii in proton-rich calcium isotopes, *Nat. Phys.* **15**, 432 (2019).

[47] P.-G. Reinhard, J. O’Neal, S. M. Wild, and W. Nazarewicz, Extended Fayans energy density functional: optimization and analysis, *J. Phys. G* **51**, 105101 (2024).

[48] J. Karthein, C. M. Ricketts, R. F. Garcia Ruiz, J. Bilowes, C. L. Binnersley, T. E. Cocolios, J. Dobaczewski, G. J. Farooq-Smith, K. T. Flanagan, G. Georgiev, W. Gins, R. P. de Groote, F. P. Gustafsson, J. D. Holt, A. Kanellakopoulos, A. Koszorús, D. Leimbach, K. M. Lynch, T. Miyagi, W. Nazarewicz, G. Neyens, P.-G. Reinhard, B. K. Sahoo, A. R. Vernon, S. G. Wilkins, X. F. Yang, and D. T. Yordanov, Electromagnetic properties of indium isotopes illuminate the doubly magic character of  $^{100}\text{Sn}$ , *Nat. Phys.* **20**, 1719 (2024).

[49] J. Dobaczewski, H. Flocard, and J. Treiner, Hartree-fock-bogolyubov description of nuclei near the neutron-drip line, *Nucl. Phys. A* **422**, 103 (1984).

[50] P.-G. Reinhard, B. Schuetrumpf, and J. Maruhn, The axial hartree-fock + bcs code skyax, *Comp. Phys. Comm.* **258**, 107603 (2021).

[51] A. Bulgac and Y.-l. Yu, Local density approximation for pairing correlations in nuclei, (2001), [arXiv:nucl-th/0109083](https://arxiv.org/abs/nucl-th/0109083).

[52] M. Bender, K. Rutz, P. G. Reinhard, and J. A. Maruhn, Pairing gaps from nuclear mean field models, *Eur. Phys. J. A* **8**, 59 (2000).